



Characterizing Superflares in HR 1099 Using Temporal and Spectral Analysis of XMM-Newton Observations

Shweta Didel¹, Jeewan C. Pandey², and A.K. Srivastava¹¹ Department of Physics, Indian Institute of Technology (BHU), Varanasi 221005, India; shwetadidel@gmail.com² Aryabhata Research Institute of Observational Sciences (ARIES), Manora Peak, Nainital 263001, India

Received 2024 October 02; revised 2024 November 11; accepted 2024 November 17; published 2024 December 23

Abstract

In the present paper, we analyze three energetic X-ray flares from the active RS CVn binary HR 1099 using data obtained from XMM-Newton. The flare duration ranges from 2.8 to 4.1 hr, with e -folding rise and decay times in the range of 27–38 minutes and 1.3–2.4 hr, respectively, indicating rapid rise and slower decay phases. The flare frequency for HR 1099 is one flare per rotation period. Time-resolved spectroscopy reveals peak flare temperatures of 39.44, 35.96, and 32.48 MK, emission measures of 7×10^{53} – 8×10^{54} cm⁻³, global abundances of 0.250, 0.299, and 0.362 Z_{\odot} , and peak X-ray luminosities of $10^{31.21}$ – $10^{32.29}$ erg s⁻¹. The quiescent state is modeled with a three-temperature plasma maintained at 3.02, 6.96, and 12.53 MK. Elemental abundances during quiescent and flaring states exhibit the inverse-first ionization potential (i-FIP) effect. We have conducted a comparative analysis of coronal abundances with previous studies and found evidence supporting the i-FIP effect. The derived flare semi-loop lengths of 6 – 8.9×10^{10} cm were found to be comparable to the other flares detected on HR 1099; however, they are significantly larger than typical solar flare loops. The estimated flare energies, ranging from $10^{35.83}$ – $10^{37.03}$ erg, classify these flares as super-flares. The magnetic field strengths of the loops are found to be in the range of 350–450 G. We diagnose the physical conditions of the flaring corona in HR 1099 through the observations of superflares and provide inference on the plasma processes.

Unified Astronomy Thesaurus concepts: RS Canum Venaticorum variable stars (1416); X-ray stars (1823); Stellar x-ray flares (1637); Stellar coronal loops (309); Stellar activity (1580); Stellar abundances (1577)

1. Introduction

Solar and stellar flares are the transient events resulting from the reconnection of magnetic loops in conjunction with the emission of radiation and particle beams, along with chromospheric evaporation, rapid mass flows, and plasma heating. From an observational perspective, flares manifest across the electromagnetic spectrum. They are characterized by a rapid rise in radiation flux, peaking at different times in various wavelengths, subsequently followed by a slow decay phase. The flares observed in the RS CVn type binary exhibit numerous similarities to the solar and other stellar flares (J. C. Pandey & K. P. Singh 2008, 2012). Nonetheless, significant differences exist in their activity indicators, including variations in the magnitude of released energy from the flaring events in the different classes of active stars. The tidal interaction between components of RS CVn binary systems can synchronize their rotational and orbital periods. Moreover, the expanded convection zone in the evolved giant or subgiant component results in much stronger magnetic activity in RS CVn binaries compared to the other late-type stars as well as the Sun. Therefore, studying flares in these cool giants and subgiants is particularly crucial, as it offers new insight into the dynamic behavior of the corona of RS CVns, which may differ significantly from that of dwarf stars.

HR 1099 (= V711 Tauri) is the RS CVn type binary (B. W. Bopp & F. Fekel 1976) located in the Taurus constellation at a distance of 29.43 ± 0.03 pc (Gaia Collaboration 2000).

Comprising a pair of solar-type stars, HR 1099 is composed of a K1IV star as primary and a smaller, rapidly rotating G5V secondary. This system exhibits a short orbital period of approximately 2.82 days (B. W. Bopp & F. Fekel 1976; F. C. J. Fekel 1983), resulting in close proximity between these two stars. One of the key features that sets HR 1099 apart is its exceptional magnetic activity. Both stars in the system generate strong magnetic fields, which in turn give rise to various physical phenomena, including surface inhomogeneity, stellar flares, X-ray emissions, and other forms of high-energy radiations, including gamma and UV radiations (e.g., D. Garcia-Alvarez et al. 2003; R. A. Osten et al. 2004). This makes HR 1099 an ideal target for studying the complex magnetic activities resulting from X-rays and other wavelengths.

HR 1099 has been extensively observed in the past from X-ray to radio wavelengths (e.g., K. G. Strassmeier & J. Bartus 2000; T. R. Ayres et al. 2001; D. Garcia-Alvarez et al. 2003; R. A. Osten et al. 2004). Many authors have done extensive analysis to identify magnetic activity cycles in HR 1099 using long-term photometry, a method known for its ability to detect changes in spot coverage. These investigations have yielded varying periods ranging from 14 to 20 yr (A. F. Lanza et al. 2006; S. V. Berdyugina & G. W. Henry 2007; S. Muneer et al. 2010). V. Perdelwitz et al. (2018) explored the long-term X-ray activity cycle and found no statistically significant periodic variations in the X-ray data set. HR 1099 is prone to X-ray flaring events (e.g., R. Nordon & E. Behar 2007; J. C. Pandey & K. P. Singh 2012; S. D. Barthelmy 2014; H. Kawai et al. 2017). The loop geometry in the corona of HR 1099 has been studied in the past reporting loop length of the order of 10^{10} cm (D. J. Mullan et al. 2006; Y. Tsuboi et al. 2016). The abundance study of the corona of HR 1099 using high-resolution spectroscopy in X-ray domain has been performed by various authors in the past, showing the



Original content from this work may be used under the terms of the [Creative Commons Attribution 4.0 licence](https://creativecommons.org/licenses/by/4.0/). Any further distribution of this work must maintain attribution to the author(s) and the title of the work, journal citation and DOI.

Table 1
Log of Observations of HR 1099

Set	Obs ID	Instruments	Start Time (UTC)	Exposure (s)	Src Radius ($''$)	Bkg Radius ($''$)	Mode	Filter	Offset ($''$)
S1	0116150601	PN	29/01/2000 15:41:01	54234	55, 15 ^a	40, 40	Full Frame	Thick	0.145
S2	0791980501	PN	25/02/2020 12:15:40	10000	60	43, 42	Small Window	Thick	0.145
		RGS	25/02/2020 01:30:57	48917					

Note.

^a These values correspond to the inner and outer radii of the chosen annular region.

presence of the inverse-first ionization potential (i-FIP) effect in the corona of this star using various plasma models like CIE, MEKAL, APEC, etc. (J. W. den Herder et al. 2001; R. A. Osten et al. 2004; D. P. Huenemoerder et al. 2013; B. Seli et al. 2022; E. Bozzo et al. 2024).

This study delves into the X-ray flares on HR 1099, utilizing data obtained from the XMM-Newton satellite. By making a detailed study of XMM-Newton observations and its X-ray spectra and light curves, we studied three superflares and derived their physical properties, loop parameters, and abundance variations. The activity level of HR 1099 appears to have remained relatively stable over time, making this type of study valuable for enhancing our understanding of the star’s physical properties. It also contributes to the long-term monitoring of superflares and provides insights into variations in their behavior.

The present paper is structured in the following manner: In Section 2, we provide details on the observations and data reduction processes. Section 3 depicts an in-depth explanation of our analysis procedures and presents the results of our X-ray temporal and spectral investigations. Lastly, in Section 4, we present discussions concerning the results and conclusive findings.

2. Observations and Data Reduction

Observations of HR 1099 were conducted using state-of-the-art instruments aboard the XMM-Newton satellite, including the European Photon Imaging Cameras (EPIC), consisting of MOS and PN cameras and the Reflection Grating Spectrometers (J. W. den Herder et al. 2001; L. Strüder et al. 2001; M. J. L. Turner et al. 2001).

HR 1099 has been observed 32 times by XMM-Newton between 2000 and 2024. After reviewing the PPS data products, we found that only 16 of these observations are suitable for analysis. Among these, six observations exhibited flares. Four of the flaring events have already been analyzed in previous studies. The log of observations, which are analyzed in this paper, is given in Table 1. We performed data reduction for the EPIC and RGS instruments using XMM-Newton’s Science Analysis System software version 21.0.0, along with the updated calibration files. To process raw EPIC data, we employed the tasks EMPROC and EPPROC for the MOS and PN data, respectively. To ensure data quality, we focused our analysis on the energy range of 0.3–10.0 keV for the EPIC data, as this range effectively minimizes high-energy background contributions. We used the task EVSELECT to identify any intervals with high background proton flare, specifically for energy levels exceeding 10 keV. All data sets were found to be free from proton flare events. Furthermore, we assessed the presence of pile-up effects using the EPATPLOT task. Significant pile-up effects were observed in the data set for observation of set S1, while no pile-up effect was detected in the case of set S2.

X-ray light curves and spectra were extracted for all PN observations by selecting circular regions centered on the source for all source counts. Background regions devoid of any source were chosen from the same CCD. The source and background radii for both the sets are mentioned in Table 1. To mitigate the pile-up effects in observation data set S1, we opted for annulus regions with inner and outer radii of 15 $''$ and 55 $''$.

All X-ray light curves obtained from PN observations underwent corrections for high background contributions and other effects using the EPICLCCORR task. Using the ESPECGET task we generated source and background spectra, along with auxiliary response files and redistribution matrix files. We employed the GRPPHA task to optimize the spectral analysis to ensure that all X-ray spectra were grouped into bins with a minimum of 20 counts each.

We conducted reduction procedures for the raw RGS data with the RGSPROC task to produce event files and other spectral products. Subsequently, we used the RGSLLCCORR and RGS COMBINE tasks to generate combined light curves and spectra for RGS1 and RGS2, respectively. These grouped spectra were then utilized for subsequent analysis.

3. Analysis and Results

In this section, we focus on analyzing the temporal and spectral characteristics of the X-ray observations.

3.1. X-Ray Light Curves

Figure 1 represents the X-ray light curves with 100 s binning, obtained from PN and RGS detectors covering the energy range 0.3–10 keV and 0.33–2.0 keV, respectively. The temporal variability of counts exhibits flare-like features with a significant increase in the count rate observed during both observations. We identified a total of three flares, namely F1, F2, and F3. The pre- and postflare time segments with nearly constant counts are referred to as P1 to P4, serving as proxies for quiescent states. All these regions are marked in Figure 1. We also used the criteria to rule out the possibility of false flare detection using only flares with a duration longer than 5 minutes and having at least five consecutive data points exceeding 3σ (H. Maehara et al. 2015, 2012). However, we were unable to analyze pixel-level data as described in H. Maehara et al. (2012) due to the broad point-spread function of XMM-Newton, with a full width at half maximum of approximately 15 $''$ for the MOS cameras and around 6.6 for the PN (L. Strüder et al. 2001; M. J. L. Turner et al. 2001). Thus, the CCDs are primarily aimed at spectral and temporal analysis rather than spatially precise, pixel-level variability studies. Additionally, as noted in Section 2, we confirmed the absence of high-energy background flares and other X-ray sources in the vicinity. The active K-type subgiant, being the primary X-ray emitter alongside a less active G-type main-sequence companion,

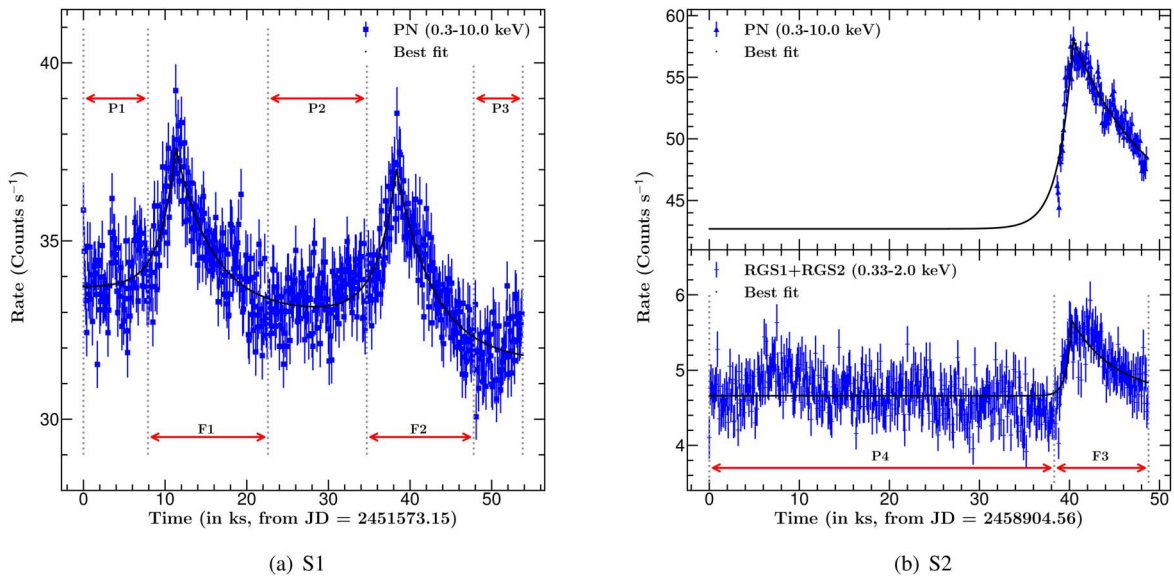


Figure 1. X-ray light curves of HR 1099 in different detectors. The flaring regions are marked by the vertical lines.

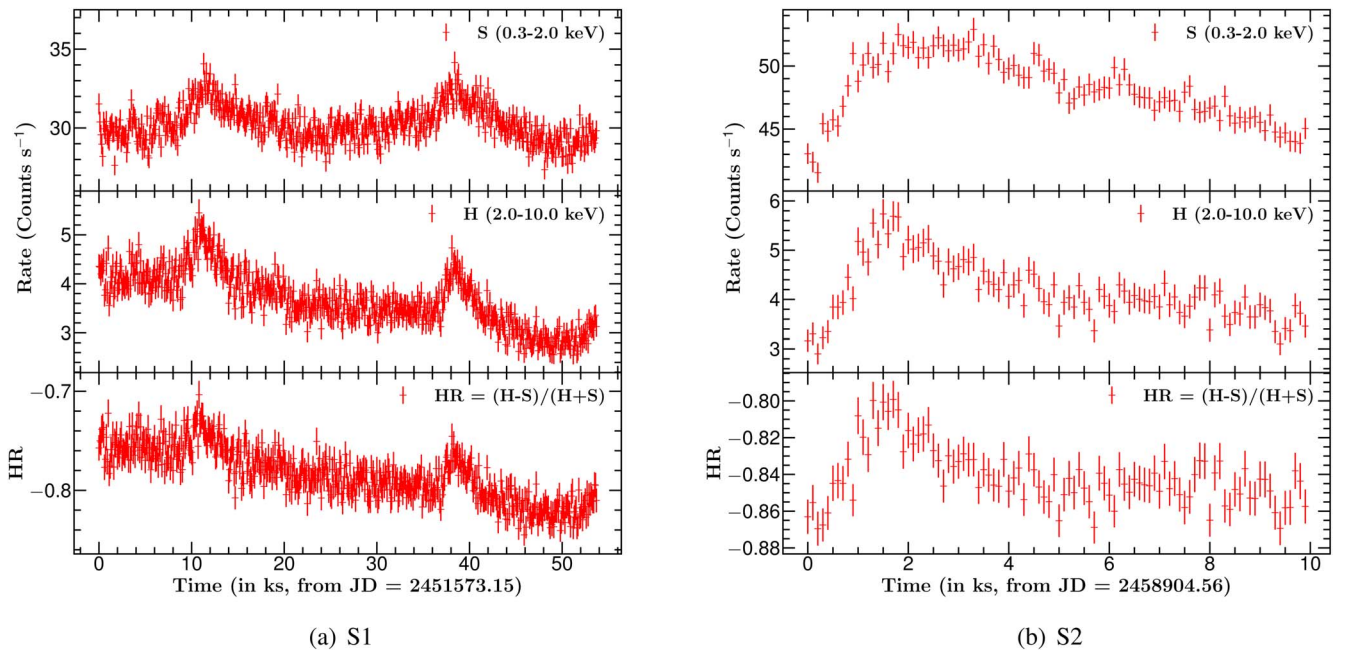


Figure 2. Soft and hard X-ray light curves along with the HR curve with 100 s binning.

rules out any flare contamination from other sources (B. W. Bopp & F. Fekel 1976; J. L. Linsky et al. 1989).

Additionally, we have plotted the light curve in two energy bands, namely soft (S; 0.2–2.0 keV) and hard (H; 2.0–10.0 keV) energy bands, along with the hardness ratio (HR), defined as $HR = (H - S)/(H + S)$, in Figure 2. The HR curve closely follows the flaring events in the light curves, indicating the rise in temperature of the X-ray emitting region with an increase in HR during the flares. The HR increase confirms the coronal heating as well as it rules out the instrumental artifacts.

Following S. Didel et al. (2024), we derived the rise and decay times for all three flares. The e -folding rise times for the flares were found to range from 1.6 to 2.3 ks, whereas the decay times ranged from 4.5 to 8.5 ks, indicating a rapid rise and slower decay pattern. Table 2 lists the rise and decay times obtained from the light curves, and Figure 1 illustrates the

modeled light curves. The peak flare count rates were increased by 16% to 36% of the quiescent state count rate in these flares.

3.2. EPIC Spectral Analysis

To monitor variations in X-ray spectral parameters across all observations, we performed X-ray spectral analysis of quiescent and flaring states separately on the PN data, as it provides a better signal-to-noise ratio. The spectral analysis was performed with Astrophysical Plasma Emission Code (APEC; R. K. Smith et al. 2001) using XSPEC, version 12.12 (K. A. Arnaud 1996). The detailed spectral analyses are described in forthcoming sections.

3.2.1. The Quiescent State Spectroscopy

For determining the quiescent temperature and emission measure, pre/postflare segments with nearly constant counts,

Table 2
The Best-fit Parameters for All the Observed Flares

Flare	Parameters			
	τ_r (ks)	τ_d (ks)	A_p (counts s ⁻¹)	A_Q (counts s ⁻¹)
S1/F1 (PN)	2.0 ± 0.2	4.5 ± 0.2	39.2 ± 0.7	33.7
S1/F2 (PN)	2.3 ± 0.2	4.6 ± 0.4	38.6 ± 0.7	33.0
S2/F3 (RGS)	0.6 ± 0.1	4.9 ± 0.7	5.9 ± 0.2	4.6
(PN)	1.6 ± 0.1	8.5 ± 0.4	58.2 ± 0.9	42.7 ^a

Notes. A_p and A_Q are the count rate of the flare peak and quiescent states, respectively.

^a Quiescent state count rates were estimated from RGS1 order 1 with an average count rate during the P4 state of 1.57 count s⁻¹ using the WebPIMMS (<https://heasarc.gsfc.nasa.gov/cgi-bin/Tools/w3pimms/w3pimms.pl>).

marked as P1 to P4, were considered as the proxy of the quiescent. For set S1, we modeled the segmented spectra from P1 to P3 using one temperature (1- T), two temperatures (2- T), three temperatures (3- T), and four-temperature (4- T) plasma models APEC with varying parameters such as temperatures, corresponding normalization parameters, and abundances. Here, we used the TBABS absorption model for hydrogen column density (N_H) and fixed it to the maximum value of galactic N_H of 10¹⁸ cm⁻² for HR 1099. We adopted solar abundances (Z_\odot) from J. Wilms et al. (2000). Abundances of all components were tied and varied together for the multi-component plasma model. The 3- T model fits the spectra well but gives varying temperatures for each P1, P2, and P3 segment. While adding one more component, the first three cool temperatures remained constant, whereas the fourth temperature varied for all the quiescent state segments. The average quiescent temperatures of cool components were found to be 0.26, 0.5, and 1.08 keV, with a weighted average temperature of 0.82 keV, calculated using the following equation

$$T_Q = \frac{\sum_{i=1}^3 T_i EM_i}{\sum_{i=1}^3 EM_i}; \quad EM_Q = \frac{1}{3} \sum_{i=1}^3 EM_i. \quad (1)$$

For set S2, the PN data included only the flare part without the pre/postflare segments throughout the observations. Therefore, we divided flare F3 into segments (rise, peak, and decay) with sufficient counts and applied the same procedure as applied for set S1. Again, the fourth temperature was found to be varying, while the first three temperatures remained nearly constant across all the segments. The coolest three temperatures were found to be similar to that for set S1 within one sigma level. Thus, for further analysis, the quiescent corona of HR 1099 was assumed to be best represented by a three-temperature plasma. All the derived spectral parameters for the quiescent states are given in Table 3.

3.2.2. Spectral Evolution During the Flares

We divided the flaring part of the light curve into distinct time intervals of rise, peak, and decay phases to understand the flare evolution. These phases are denoted as R_i , P , and D_i , where the index “ i ” can take values from 1 onwards. The duration of each flare segment was chosen to ensure an equal number of counts within each interval.

We applied a consistent approach for all flares analyzed here. Each segmented spectrum was modeled using a 4- T APEC model. The temperatures and emission measures of the first three plasma components were fixed at their corresponding quiescent values,

allowing the parameters of the fourth component to vary in order to obtain the flare-specific parameters. The parameters derived for each flare are given in Table 4. The temporal variations of these parameters are illustrated in Figure 3, demonstrating that nearly all parameters peak during the peak phase of the flare. The peak flare temperature, kT_4 , was found to be 3.4, 3.1, and 2.8 keV, while the peak emission measure, EM_4 , reached 7.1, 7.0, and 81×10^{53} cm⁻³ for flares F1, F2, and F3, respectively. We determined the unabsorbed flux for each flare segment using the convolution model CFLUX and integrated this flux across all segments to obtain the total flux (F). From this, we derived the luminosity ($L_{XF} = 4\pi D^2 F$) and the total flare energy ($E_{X,Total} = L_{XF} \times (\tau_r + \tau_d)$), where D represents the distance to the object in cm. The resulting values for L_{XF} and $E_{X,Total}$ are presented in Table 6. The peak abundance (Z) and the peak X-ray luminosity (L_{XF}) of flares were found to be 0.25, 0.299, and 0.362 Z_\odot and $10^{31.21}$, $10^{31.23}$, and $10^{32.29}$ erg s⁻¹ for the flare F1, F2, and F3, respectively. We found that temperature peaked either earlier than the emission measure or simultaneously with the emission measure. The abundance peaked after the emission measure for flares F1 and F3, whereas for flare F2, it peaked with the emission measure and remained constant thereafter for the initial phase of the flare decay.

3.3. RGS Spectral Analysis

The RGS1 and RGS2 spectra for set S2 were generated for both the quiescent state (P4) and the flaring state (F3) and fitted with the VAPEC model. Additionally, the TBABS model was used to account for the N_H , which was fixed to a minimum value of 10¹⁸ cm⁻². All temperatures and corresponding emission measures were left as free parameters for the quiescent state spectral fitting. The abundances of He, Ni, and Al were set to the solar photospheric values, while the other abundances were allowed to vary and were tied among each temperature component. We found that a 3- T plasma model provided the best fit for the P4 quiescent segment.

For the flaring spectra, a 4- T VAPEC model was used for the fitting. The first three temperatures and corresponding normalization parameters were fixed at the quiescent values as obtained from spectral fitting of the P4 region, and all abundances were tied among the different components. Table 5 represents the best-fit model parameters for both the quiescent and flaring phases within a 68% confidence interval.

In Figure 4, we present the RGS1 and RGS2 spectra of HR 1099 for flare F3 and its pre-flare state P4, including emission lines from various elements. The best-fit thermal plasma model, VAPEC, is illustrated with solid lines for both the flare and quiescent states. The residuals of the best-fit model are shown in the lower panel.

3.3.1. First Ionization Potential (FIP) and Inverse-FIP Effect

Due to fractionation processes associated with the FIP, the elemental abundances in the corona differ from those in the underlying photosphere. In less active slow rotators like the Sun, elements with FIP < 10 eV are generally enhanced compared to those with FIP > 10 eV, a phenomenon termed the FIP effect (U. Feldman 1992; J. M. Laming et al. 1995; U. Feldman & J. M. Laming 2000). On the other hand, fast-rotating stars, which exhibit higher magnetic activity, often show an i-FIP effect (see J. M. Laming 2015, 2021). Some stars with magnetically inactive chromospheres show no detectable FIP bias (J. J. Drake et al. 1994).

Table 3
Spectral Parameters of the Quiescent Using 4-*T* APEC Model for All the Data Sets, within a 68% Confidence Range

Set	Para											χ^2_{ν} (dof)
	kT_1	kT_2	kT_3	kT_4	T_Q^a	EM ₁	EM ₂	EM ₃	EM ₄	EM _Q ^a	Z	
	(keV)					$(10^{53} \text{ cm}^{-3})$					(Z_{\odot})	
S1	$0.26^{+0.03}_{-0.03}$	$0.5^{+0.1}_{-0.1}$	$1.08^{+0.03}_{-0.02}$	$2.3^{+0.1}_{-0.09}$	$0.82^{+0.06}_{-0.05}$	$1.4^{+0.4}_{-0.5}$	$0.8^{+0.5}_{-0.4}$	$3.9^{+0.4}_{-0.3}$	$5.9^{+0.3}_{-0.3}$	$2.0^{+0.3}_{-0.2}$	$0.26^{+0.03}_{-0.03}$	1.09 (566)
S2	$0.26^{+0.02}_{-0.02}$	$0.59^{+0.09}_{-0.08}$	$1.07^{+0.04}_{-0.03}$	$2.6^{+0.2}_{-0.1}$	$0.8^{+0.1}_{-0.1}$	29^{+3}_{-4}	15^{+5}_{-4}	70^{+7}_{-7}	64^{+6}_{-6}	38^{+3}_{-3}	$0.34^{+0.03}_{-0.03}$	1.14(502)

Note.

^a For the calculation of T_Q and EM_Q, only the first three temperatures and emission measures have been used.

Table 4.
Best-fit Spectral Parameters for Each Time Segment During the Flares F1 to F3 within 68% Confidence Interval

Flare	Flare Segments	Parameters					χ^2_{ν} (dof)
		kT_4 (keV)	EM ₄ $(10^{53} \text{ cm}^{-3})$	Z (Z_{\odot})	L_{XF} $(10^{31} \text{ erg s}^{-1})$		
F1	R1	$3.4^{+0.1}_{-0.1}$	$5.7^{+0.2}_{-0.2}$	$0.217^{+0.007}_{-0.007}$	$1.421^{+0.009}_{-0.009}$	1.12 (416)	
	R2	$3.3^{+0.1}_{-0.1}$	$6.0^{+0.2}_{-0.2}$	$0.228^{+0.009}_{-0.009}$	$1.46^{+0.01}_{-0.01}$	1.08 (372)	
	P	$3.4^{+0.1}_{-0.1}$	$7.1^{+0.2}_{-0.2}$	$0.233^{+0.009}_{-0.009}$	$1.62^{+0.01}_{-0.01}$	1.16 (395)	
	D1	$3.32^{+0.1}_{-0.09}$	$6.9^{+0.2}_{-0.2}$	$0.250^{+0.009}_{-0.009}$	$1.60^{+0.01}_{-0.01}$	1.14 (386)	
	D2	$3.29^{+0.09}_{-0.08}$	$6.5^{+0.2}_{-0.2}$	$0.246^{+0.009}_{-0.009}$	$1.53^{+0.01}_{-0.01}$	1.02 (388)	
	D3	$3.0^{+0.1}_{-0.1}$	$6.2^{+0.2}_{-0.2}$	$0.238^{+0.009}_{-0.008}$	$1.47^{+0.01}_{-0.01}$	1.04 (377)	
	D4	$2.9^{+0.1}_{-0.1}$	$6.0^{+0.2}_{-0.2}$	$0.24^{+0.01}_{-0.01}$	$1.45^{+0.01}_{-0.01}$	1.05 (346)	
F2	R1	$2.51^{+0.09}_{-0.09}$	$6.0^{+0.2}_{-0.2}$	$0.267^{+0.009}_{-0.009}$	$1.43^{+0.01}_{-0.01}$	1.0 (371)	
	R2	$2.57^{+0.09}_{-0.09}$	$6.3^{+0.2}_{-0.2}$	$0.281^{+0.009}_{-0.009}$	$1.49^{+0.01}_{-0.01}$	0.97 (375)	
	P	$3.1^{+0.1}_{-0.1}$	$7.0^{+0.2}_{-0.2}$	$0.299^{+0.009}_{-0.009}$	$1.68^{+0.01}_{-0.01}$	1.05 (405)	
	D1	$2.7^{+0.1}_{-0.1}$	$6.5^{+0.2}_{-0.2}$	$0.293^{+0.009}_{-0.01}$	$1.55^{+0.01}_{-0.01}$	1.08 (372)	
	D2	$2.5^{+0.1}_{-0.1}$	$6.2^{+0.2}_{-0.2}$	$0.297^{+0.01}_{-0.009}$	$1.50^{+0.01}_{-0.01}$	0.96 (362)	
	D3	$2.41^{+0.08}_{-0.08}$	$5.8^{+0.2}_{-0.2}$	$0.27^{+0.01}_{-0.01}$	$1.41^{+0.01}_{-0.01}$	1.04 (357)	
	D4	$2.4^{+0.1}_{-0.1}$	$5.3^{+0.2}_{-0.2}$	$0.291^{+0.009}_{-0.009}$	$1.39^{+0.01}_{-0.01}$	1.15 (359)	
F3	D5	$2.3^{+0.1}_{-0.1}$	$5.1^{+0.2}_{-0.2}$	$0.286^{+0.009}_{-0.009}$	$1.34^{+0.01}_{-0.01}$	0.93 (363)	
	R	$2.64^{+0.08}_{-0.07}$	60^{+2}_{-1}	$0.331^{+0.006}_{-0.006}$	$16.83^{+0.01}_{-0.01}$	1.17 (489)	
	P	$2.80^{+0.07}_{-0.06}$	81^{+2}_{-2}	$0.344^{+0.006}_{-0.006}$	$19.40^{+0.01}_{-0.01}$	1.09 (544)	
	D1	$2.59^{+0.07}_{-0.07}$	71^{+2}_{-2}	$0.362^{+0.007}_{-0.007}$	$18.55^{+0.01}_{-0.01}$	1.13 (519)	
	D2	$2.52^{+0.07}_{-0.06}$	65^{+2}_{-2}	$0.358^{+0.007}_{-0.007}$	$17.53^{+0.01}_{-0.01}$	1.17 (495)	
	D3	$2.45^{+0.06}_{-0.06}$	63^{+2}_{-1}	$0.342^{+0.006}_{-0.006}$	$17.16^{+0.01}_{-0.01}$	1.12 (509)	
	D4	$2.46^{+0.06}_{-0.06}$	63^{+2}_{-1}	$0.323^{+0.006}_{-0.006}$	$16.80^{+0.01}_{-0.01}$	1.12 (509)	

The measured abundances as a function of FIP, for both quiescent and flaring phases are shown in Figure 7. The elements with FIP < 10 eV like Mg, Fe, and Si were found to be under-abundant relative to the solar photospheric values in both states, with values of approximately ~ 0.44 , ~ 0.26 , and ~ 0.70 for the quiescent state, and ~ 0.48 , ~ 0.28 , and ~ 0.86 for the flaring state, respectively. Additionally, the abundances of N, O, and Si are lower in the quiescent state compared to the flaring state, while the remaining abundances are similar to the flaring values within a 68% confidence interval. Thus, the evidence of the i-FIP effect is observed in HR 1099 in the case of both the quiescent and flaring states in the present observational baseline.

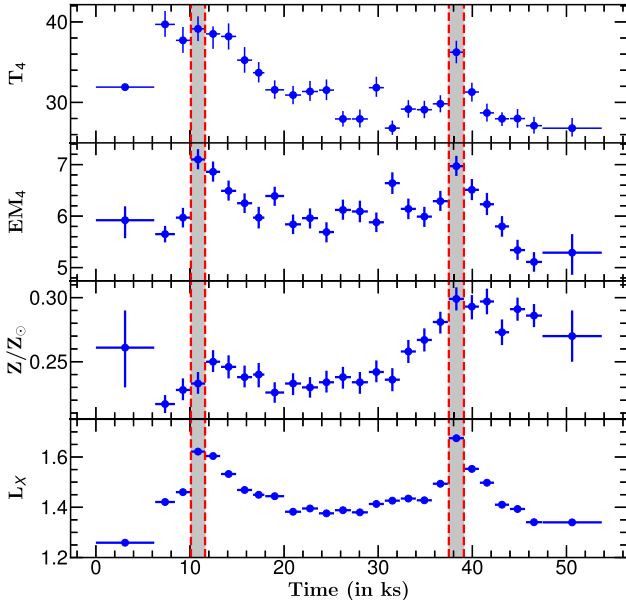
3.4. Loop Modeling

Loop length is an essential parameter for determining the physical size of flaring loops and the star's corona. Although stellar flares are spatially unresolved, analogies with the solar flares and loop models allow us to infer the coronal geometry. During a heating event, the temperature of the loop increases

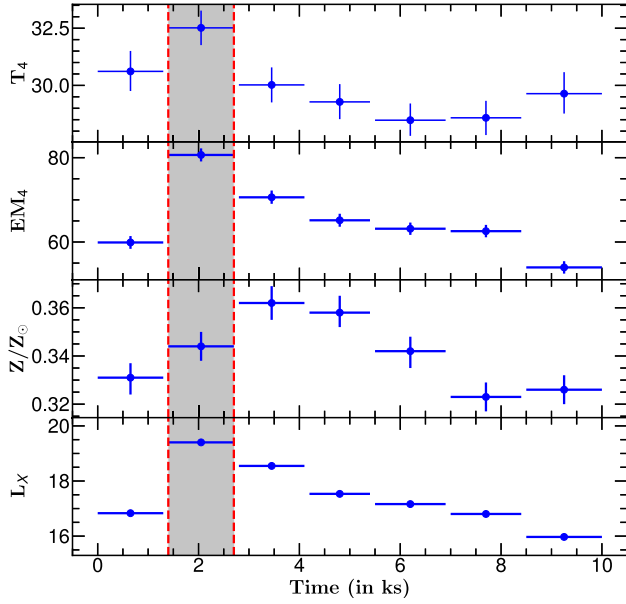
and peaks at temperature T_0 , while chromospheric evaporation causes an increase in the density. Throughout the decay phase, the thermal conduction cooling becomes dominant, leading to a temperature drop during this stage of the flare. This cooling phase provides valuable insights into the energy release and transport mechanisms within the stellar corona. Using the hydrodynamic loop model, F. Reale et al. (1997) derived a relation for the semiloop length of the flaring loops. This model assumes a dominant single coronal loop and incorporates both plasma cooling and heating effects during the flare's decay phase. The hydrodynamic model helps to understand the balance between conductive and radiative cooling processes. The semiloop length (L) is given by F. Reale et al. (1997):

$$L = 2.7 \times 10^3 \frac{\tau_d T_{\max}^{1/2}}{F(\zeta)} \text{ cm for } 0.35 < \zeta \leq 1.6 \quad (2)$$

$$\text{with } F(\zeta) = \frac{0.51}{\zeta - 0.35} + 1.36, \text{ and } T_{\max} = 0.13T_0^{1.16}. \quad (3)$$



(a) S1



(b) S2

Figure 3. The temporal variation of spectral parameters T_4 , EM_4 , Z , and Luminosity L_{XF} for sets S1 and S2. The T_4 is in units of MK, EM_4 in 10^{53} cm^{-3} , L_{XF} in $10^{31} \text{ erg s}^{-1}$. The shaded regions show the peak phase of the corresponding flare.

Here, τ_d is the decay time in s, $F(\zeta)$ is the correction factor accounting for the heating, and ζ is the slope of the best-fit straight line of $\log(\sqrt{\text{EM}})$ versus $\log(T)$ diagram during the decay phase of the flare. Figure 5 shows $\log(\sqrt{\text{EM}})$ versus $\log(T)$ diagram (equivalent to the density versus temperature diagram) for all three flares along with the best-fit straight line and corresponding ζ values. The value of ζ in the range of 0.36–1.6 suggests sustained heating during the flare’s slow decay phase (see F. Reale 2007 for detail). For flare F1 and F2, the value of ζ is above the critical value but well with a 1σ level, whereas for flare F3, ζ was found to be 1.03 ± 0.07 . These values indicate the non-negligible heating during the decay phase of the observed flares.

Table 5

The Best-fit Optimal Spectral Parameters Derived from Fitting the RGS Spectra within a 68% Confidence Level

Parameters	Segments	
	P4 Z/Z_\odot	F3 Z/Z_\odot
kT_1 (keV)	$0.39^{+0.01}_{-0.02}$
kT_2 (keV)	$0.83^{+0.01}_{-0.02}$
kT_3 (keV)	$1.74^{+0.05}_{-0.05}$
kT_4 (keV)	$1.9^{+1.4}_{-0.4}$
EM_1 (10^{53} cm^{-3})	$1.02^{+0.06}_{-0.09}$
EM_2 (10^{53} cm^{-3})	$2.27^{+0.09}_{-0.09}$
EM_3 (10^{53} cm^{-3})	$4.6^{+0.1}_{-0.1}$
EM_4 (10^{53} cm^{-3})	$1.08^{+0.05}_{-0.03}$
C	$1.0^{+0.1}_{-0.1}$	$1.1^{+0.1}_{-0.1}$
N	$0.55^{+0.09}_{-0.09}$	$0.95^{+0.07}_{-0.07}$
O	$0.72^{+0.03}_{-0.03}$	$0.79^{+0.01}_{-0.02}$
Ne	$1.50^{+0.08}_{-0.07}$	$1.63^{+0.07}_{-0.07}$
Mg	$0.44^{+0.05}_{-0.05}$	$0.48^{+0.04}_{-0.04}$
Si	$0.70^{+0.07}_{-0.07}$	$0.86^{+0.07}_{-0.07}$
S	$0.38^{+0.1}_{-0.09}$	$0.49^{+0.09}_{-0.09}$
Ar	$0.9^{+0.2}_{-0.2}$	$1.3^{+0.2}_{-0.2}$
Fe	$0.26^{+0.01}_{-0.01}$	$0.28^{+0.04}_{-0.04}$
χ^2_ν	1.41	1.19
(dof)	2502	1249

Note. All the elemental abundances are in terms of solar photospheric abundances taken from J. Wilms et al. (2000).

The T_0 is the maximum best-fit segmented average temperature derived from the spectral fitting in units of K, whereas (T_{max}) is the maximum temperature of the flare calculated using the Equation (3). The T_{max} for the flare F1, F2, and F3 were found to be 84 ± 3 , 76 ± 3 , and 67 ± 2 MK, respectively.

The derived loop lengths were found to be in the range $5.9\text{--}8.9 \times 10^{10}$ cm as given in Table 6. Assuming a single cylindrical loop with half loop length L , we have derived some more physical parameters like loop volume (V), plasma density (n_e), plasma pressure at loop apex (P), the minimum magnetic field required to confine the plasma inside the flaring loop (B_{min}), total magnetic field (B_{Total}), heating rate (E_{HR}), and the total energy related to the heating rate ($E_{\text{H,Total}}$). S. Didel et al. (2024) have also performed such estimations for the corona of AB Dor. All these parameters are mentioned in Table 6.

4. Discussion and Conclusions

Our study of the active RS CVn binary HR 1099 provides a detailed analysis of the three energetic X-ray flares. The duration of these flares is found in the range of 2.8–4.1 hr. The flare duration of these three flares is in between the flare duration observed in other flares in HR 1099, which were in the range of 1–9 hr (M. Audard et al. 2001; R. A. Osten et al. 2004; R. Nordon & E. Behar 2007; J. C. Pandey & K. P. Singh 2012). However, these flares are of very short duration in comparison to the longest duration flares observed in HR 1099 on two different occasions, with a flare duration of >2.3 and ~ 2.8 days, respectively (U. Feldman & J. M. Laming 2000; S. Karmakar 2024).

Our analysis further explores the e -folding rise and decay times of these flares, revealing the rise time ranging from 10 to 38 minutes and decay time from 1.25 to 2.4 hr. This pattern of a

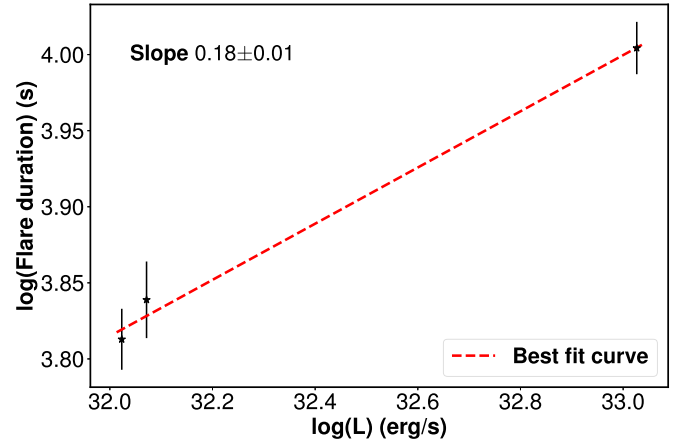
Table 6
Loop Parameters

Parameters	Flare		
	F1	F2	F3
L_{XF} (10^{31} erg s^{-1})	10.55 ± 0.03	11.79 ± 0.03	106.3 ± 0.2
$E_{X,Total}$ (10^{35} erg)	6.8 ± 0.3	8.1 ± 0.5	107 ± 4
T_0 (MK)	39 ± 1	36 ± 1	32.5 ± 0.8
T_{max} (MK)	84 ± 3	76 ± 3	67 ± 2
L (10^{10} cm)	>6.0	>5.9	8.9 ± 0.5
h/R_*	>0.14	>0.14	0.21 ± 0.01
V (10^{31} cm 3)	>1.36	>1.29	4.4 ± 0.8
n_e (10^{11} cm $^{-3}$)	<2.5	<2.6	4.8 ± 0.4
P (10^3 dyne cm $^{-2}$)	<5.3	<4.9	8.0 ± 0.7
B_{min} (G)	<364	<351	448 ± 20
B_{Total} (G)	-608	-558	530 ± 28
E_{HR} (10^{31} erg s^{-1})	-2.0	-1.4	1.4 ± 0.2
$E_{H,Total}$ (10^{35} erg)	-1.3	-1.0	1.4 ± 2
M_{CME} (10^{19} g)	-3.04	-3.25	-14.5

Note. Here, loop height, $h = 2L/\pi$ and R_* is the radius of the star.

The quiescent state of HR 1099 is characterized by a four-temperature plasma, in which the coolest three temperatures represent the quiescent state of HR 1099 with values of 3.02, 6.96, and 12.53 MK and an average temperature of 9.4 MK. The presence of a fourth temperature during the pre- and postflare state could be due to the presence of flaring components as both flares F1 and F2 are observed one after another. From high-resolution X-ray spectra, the three-temperature quiescent state was modeled using VAPEC with temperatures 4.5, 9.6, and 20.2 MK with a weighted average temperature of 15.1 MK and average EM of 2.6×10^{53} cm $^{-3}$; the average quiescent temperature and EM is found to be similar to the previous results with 4- T quiescent as reported by M. Audard et al. (2001, 2003) with values nearly 17 MK and 2- T quiescent by R. A. Osten et al. (2004) with values 18.6 MK and 4×10^{53} cm $^{-3}$. However, E. Bozzo et al. (2024) reported the 4- T quiescent with lower plasma parameters like the average temperature of 6 MK whereas average EM of 1.3×10^{52} cm $^{-3}$.

The TRS of the flaring spectra provides detailed insights into the physical processes occurring within the flaring region and helps to understand the flare evolution. According to the general flare evolution scenario, a heat pulse causes a rapid increase in the temperature throughout the loop. This heat is conducted from the hot regions to the cooler chromosphere, causing the chromospheric plasma to expand upward and evaporate explosively. Once the evaporation rate slows down, it balances with cooling, and the plasma cools rapidly through conduction while its density increases. Eventually, radiative cooling becomes more effective than conduction, causing the density to peak and the loop to start to deplete. Radiative cooling then becomes the dominant cooling mechanism (S. Serio et al. 1991; F. Reale 2007, 2014). The observed increment in coronal loop temperature, plasma density, and abundance resembles the plasma heating and chromospheric evaporation scenario in the observed flaring loops. Meanwhile, during the decay phase of the flare, the decrease in these parameters indicates the cooling mechanism with sustained heating. However, in the present case, due to the limited time resolution, we could observe that the temperature peaked either during the rising phase or simultaneously peaked with the

**Figure 6.** Log-log plot of flare duration vs. luminosity with linear curve fit.

luminosity and emission measure or at the peak phase of the flares. However, the abundances peaked after the emission measure peak, which is evidence of chromospheric evaporation.

The TRS results show averaged peak temperatures of 39.44, 35.96, and 32.48 MK, emission measures of 7, 7, and 81×10^{53} cm $^{-3}$ for flares F1, F2, and F3, respectively. Further, we found the global abundances of 0.250, 0.299, and 0.362 Z_{\odot} , peak X-ray luminosities (L_{XF}) of 1.62, 1.68, and 19.40×10^{31} erg s^{-1} , and total flare energy of 6.8×10^{35} , 8.1×10^{35} , and 1.07×10^{37} erg. These results show similarity with the past results for this active star observed with various instruments like EUVE, MAXI, Chandra, Swift, etc. (D. J. Mullan et al. 2006; R. Nordon & E. Behar 2007; Y. Tsuboi et al. 2016; S. Karmakar 2024). A. Veronig et al. (2002), S. Christe et al. (2008), and Y. Tsuboi et al. (2016) established a relationship between flare duration and total flare luminosity, expressed as $\tau \propto L_{XF}^{\alpha}$, where α represents the slope of the log-log plot of flare duration (τ) versus luminosity (L_{XF}). Based on data from the Sun and nearby stars, they reported slopes of approximately 0.33, 0.2, and 0.2 ± 0.03 for energy ranges of 3.1–24.8 keV, 6–12 keV, and 0.1–100 keV, respectively. Additionally, H. Maehara et al. (2015) and A. K. Althukair & D. Tsiklauri (2023a) reported a similar relationship using optical data from the KEPLER mission. Using our limited data sample, we obtained a slope of 0.18 ± 0.01 in the energy range of 0.3–10.0 keV, as shown in Figure 6.

The elemental abundances provide detailed information about the physical nature of the plasma present in the coronae of the stars. The individual abundances during both the quiescent and flaring states in the coronal loops of HR 1099 exhibit the i-FIP effect, a phenomenon also observed in other magnetically active stars (A. C. Brinkman et al. 2001; B. Seli et al. 2022). The FIP and i-FIP effects in the active stars have been explained in detail by J. M. Laming et al. (2019). The ponderomotive force associated with the Alfvén waves and fast mode waves separates ions from neutrals in the chromospheric regions, which can explain the physical mechanism responsible for such effects (J. M. Laming 2021; A. S. H. To et al. 2021; and references therein). The resonant Alfvén waves propagating along coronal loops can result in the FIP effect, while the i-FIP effect can be reasonably explained by upward-propagating p modes. The magneto-acoustic waves or p modes convert to fast modes and propagate into the low-plasma-beta ($\beta < 1$) regions (J. M. Laming 2015, 2021; D. Baker et al. 2019). Such plasma processes can also be attributed as a physical cause of

Table 7
Abundances of the Elements with Respect to Fe in the Corona of HR 1099 along with the other Observations Taken from the Literature

Elements	P4	F3	Z (a)	Z (b)	Z (c)	Z (d)	Z (e)	Z (f)
					Flare/Quiescent			
[C/Fe]	4.4 ± 0.5	4.6 ± 0.7	$4.0 \pm 0.3/3.1 \pm 0.3$...	2.75 ± 0.6	...
[N/Fe]	2.5 ± 0.4	4.0 ± 0.6	$3.3 \pm 0.2/2.6 \pm 0.3$	4.37 ± 0.3	4.1 ± 0.8	...
[O/Fe]	2.7 ± 0.2	2.8 ± 0.4	...	3 ± 0.1	$1.81 \pm 0.05/1.5 \pm 0.1$	2.63 ± 0.06	2.75 ± 0.5	1.75 ± 0.8
[Ne/Fe]	7.1 ± 0.4	7.2 ± 0.9	8.2 ± 0.5	9.77 ± 0.1	$3.4 \pm 0.2/2.7 \pm 0.3$	7.59 ± 0.2	6.6 ± 1.1	8.67 ± 2.5
[Mg/Fe]	1.9 ± 0.2	2.0 ± 0.3	2.0 ± 0.1	2.5 ± 0.1	$2.2 \pm 0.2/3.0 \pm 0.5$	1.55 ± 0.04	0.9 ± 0.3	2.42 ± 0.9
[Si/Fe]	2.5 ± 0.3	2.8 ± 0.4	1.8 ± 0.1	1.9 ± 0.1	$2.0 \pm 0.1/2.2 \pm 0.4$	1.51 ± 0.04	1.1 ± 0.3	2.17 ± 0.7
[S/Fe]	1.9 ± 0.5	2.3 ± 0.5	1.6 ± 0.2	1.48 ± 0.2	$1.6 \pm 0.1/<1.2$	1.51 ± 0.07	0.5 ± 0.4	2.58 ± 0.9
[Ar/Fe]	4.3 ± 0.9	6 ± 1 / ...	4.7 ± 0.4	2.5 ± 1.3	4.0 ± 1.9

Note. All the values are expressed relative to the solar photospheric abundances (E. Anders & N. Grevesse 1989). **References.** (a) E. Bozzo et al. (2024); (b) J. J. Drake et al. (2001); (c) R. Nordon & E. Behar (2008); (d) D. P. Huenemoerder et al. (2013); (e) M. Audard et al. (2003); (f) R. A. Osten et al. (2004).

the FIP and i-FIP effects observed presently in the flaring epoch of the localized corona of HR 1099.

The i-FIP effect in HR 1099 has also been previously reported (A. C. Brinkman et al. 2001; J. J. Drake et al. 2001; R. Nordon & E. Behar 2008; B. Seli et al. 2022). In this study, we provide a comparative analysis of the coronal elemental abundances and the i-FIP effect in the coronal loop plasma of HR 1099 with the other estimations existing in the previous literature. The coronal abundances (Z/Z_{\odot}) relative to Fe are presented in Table 7 and Figure 7 for P4 and flare F3, alongside previously reported values obtained from various instruments. In this study, we assumed the photospheric values of HR 1099 to be analogous to those of the solar photosphere. Here, we assumed the photospheric values of HR 1099 to be analogous to those of the solar photosphere. The derived values of abundance are found to be consistent with the past literature values. However, the abundances of Fe and Ne as derived by R. Nordon & E. Behar (2007) exhibit lower values compared to those derived in other studies. The Fe and O abundances align closely with earlier reports, with minimal uncertainty, making the Fe/O ratio a useful indicator of the FIP bias in coronal abundances (B. E. Wood & J. L. Linsky 2010; B. E. Wood et al. 2012). A lower Fe/O ratio signifies a stronger i-FIP effect in the star's corona. The Fe/O abundance ratio during the quiescent state P4 and flaring state F3 of HR 1099 were found to be 0.36 ± 0.02 and 0.35 ± 0.05 , respectively. These values are consistent with previously reported values between 0.3 and 0.7 for HR 1099, as shown in Table 7. In other active RS CVn binaries, the Fe/O ratio varies based on the star's activity level and spectral type (UX Ari, λ And, VY Ari, Capella etc.; M. Audard et al. 2003; R. Nordon & E. Behar 2007; B. Seli et al. 2022).

We derived the semiloop lengths of the flares using the hydrodynamic loop model, finding them to range between 5.9 and 8.9×10^{10} cm. In comparison, typical loop lengths for solar flares are of the order of 10^9 – 10^{10} cm. The loop heights ($h = 2L/\pi$) corresponding to these semiloop lengths constitute a small fraction of the radius of HR 1099. The h/R_{\star} ratios for these flares were found to be 0.14 for both F1 and F2 and 0.21 for the flare F3. D. J. Mullan et al. (2006) reported the value of L and the ratio h/R_{\star} in the range of 4.8 – 12.7×10^{10} cm and 0.1 to 0.3 for HR 1099.

The total X-ray energy released during the flares was estimated to be between 6.8×10^{35} and 10.7×10^{36} erg, which is substantially higher than the total energy of the most powerful solar flares (A. G. Emslie et al. 2012; I. V. Zimovets et al. 2020). The calculated loop volume V , electron density n_e ,

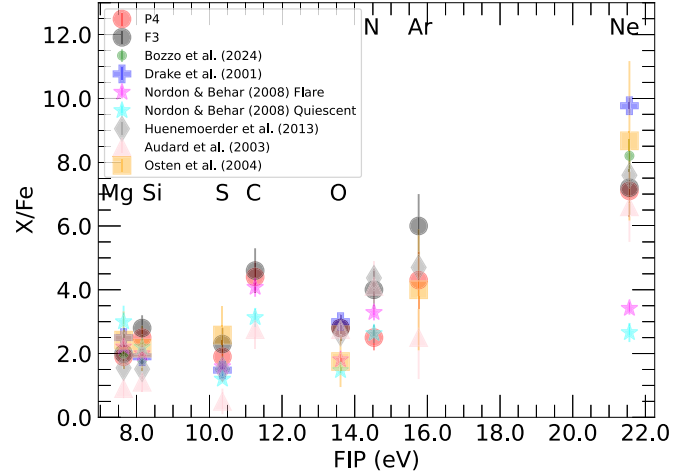


Figure 7. All the elemental abundances relative to Fe are plotted against the first ionization potential (FIP). The values are provided in Table 7.

and plasma pressure P were found to be in the range of 1.3 – 4.4×10^{31} cm $^{-3}$, 2.5 – 4.8×10^{11} cm $^{-3}$, and 5 – 8×10^3 dyne cm $^{-2}$. Additionally, the total magnetic field strength B_{Total} of the loops was found to be between 500 and 600 G, similar to typical magnetic field observations for HR 1099 (D. J. Mullan et al. 2006; J. C. Pandey & K. P. Singh 2012) and the minimum magnetic field B_{min} in the range of 350–448 G (110–320 G; D. J. Mullan et al. 2006).

The mass of ejected CME associated with the flare can be estimated with the relation $M_{\text{CME}}(g) = 10^{-1.5 \pm 0.5} E_G^{0.59 \pm 0.02}$, where E_G is the energy released during the flare in GOES (1–8 Å) energy band (A. N. Aarnio et al. 2012; J. J. Drake et al. 2013), which can be converted from XMM-Newton flux from 0.3 to 10.0 keV band to GOES flux using WEBPIMMS. The M_{CME} for HR 1099 was found to be in the range of approximately 3.0 – 14.5×10^{19} g, which was found to be maximum for flare F3 as mentioned in Table 6. These values are approximately 100 to 1000 times higher than the most massive solar CME reported (S. Yashiro & N. Gopalswamy 2009). However, they exceed the mass of CMEs observed on other active stars such as AB Dor, EQ Peg, EK Dra, etc., which have typical CME masses in the range of 10^{18} – 10^{19} g (K. Namekata et al. 2021; S. Karmakar et al. 2022; S. Didel et al. 2024). Based on the calculated parameters for HR 1099 using X-ray data, such as flare temperature, emission measure, loop length, magnetic field, etc., it is evident that the study of flare parameters plays a crucial role in understanding the

coronal dynamics of the magnetically active stars. The more resolved data and multiwavelength perspective can provide a comprehensive understanding of the geometry of the corona and the physical processes happening during these flares in detail.

Acknowledgments

This work presented here is based on the observations of the XMM-Newton satellite, an ESA science mission with instruments and contributions directly funded by ESA Member States and NASA. S.D. acknowledges the CSIR funding agency for providing the research grant. A.K.S. acknowledges the support of the ISRO project in facilitating this scientific research. We thank the reviewer for reading our paper and giving us useful comments.

Data Availability

The data utilized in this paper is accessible through the XMM-Newton archive.

ORCID iDs

Jeewan C. Pandey  <https://orcid.org/0000-0002-4331-1867>
A.K. Srivastava  <https://orcid.org/0000-0002-1641-1539>

References

- Aarnio, A. N., Matt, S. P., & Stassun, K. G. 2012, *ApJ*, **760**, 9
 Althukair, A. K., & Tsiklauri, D. 2023a, *RAA*, **23**, 085017
 Althukair, A. K., & Tsiklauri, D. 2023b, *RAA*, **23**, 105010
 Anders, E., & Grevesse, N. 1989, *GeCoA*, **53**, 197
 Arnaud, K. A. 1996, in ASP Conf. Ser. 101, *Astronomical Data Analysis Software and Systems V*, ed. G. H. Jacoby & J. Barnes (San Francisco, CA: ASP), 17
 Audard, M., Güdel, M., & Mewe, R. 2001, *A&A*, **365**, L318
 Audard, M., Güdel, M., Sres, A., Raassen, A. J. J., & Mewe, R. 2003, *A&A*, **398**, 1137
 Ayres, T. R., Brown, A., Osten, R. A., et al. 2001, *ApJ*, **549**, 554
 Baker, D., van Driel-Gesztelyi, L., Brooks, D. H., et al. 2019, *ApJ*, **875**, 35
 Barthelmy, S. D. 2014, *GCN*, 15679, 1
 Berdyugina, S. V., & Henry, G. W. 2007, *ApJL*, **659**, L157
 Bopp, B. W., & Fekel, F. 1976, *AJ* 1976, **81**, 771
 Bozzo, E., Huenemoerder, D. P., Falanga, M., et al. 2024, *MNRAS*, **528**, 4591
 Brinkman, A. C., Behar, E., Güdel, M., et al. 2001, *A&A*, **365**, L324
 Christe, S., Hannah, I. G., Krucker, S., McTiernan, J., & Lin, R. P. 2008, *ApJ*, **677**, 1385
 den Herder, J. W., Brinkman, A. C., Kahn, S. M., et al. 2001, *A&A*, **365**, L7
 Didel, S., Pandey, J. C., Srivastava, A. K., & Singh, G. 2024, *MNRAS*, **527**, 1705
 Drake, J. J., Brickhouse, N. S., Kashyap, V., et al. 2001, *ApJL*, **548**, L81
 Drake, J. J., Cohen, O., Yashiro, S., & Gopalswamy, N. 2013, *ApJ*, **764**, 170
 Drake, J. J., Laming, J. M., Widing, K. G., et al. 1994, *AAS Meeting Abstracts*, 184, 05.22
 Emslie, A. G., Dennis, B. R., Shih, A. Y., et al. 2012, *ApJ*, **759**, 71
 Fekel, F. C. J. 2013, *ApJ*, **268**, 274
 Feldman, U. 1992, *PhysS*, **46**, 202
 Feldman, U., & Laming, J. M. 2000, *PhysS*, **61**, 222
 Gaia Collaboration 2020, *yCat*, I/350
 Garcia-Alvarez, D., Foing, B. H., Montes, D., et al. 2003, *A&A*, **397**, 285
 Huenemoerder, D. P., Phillips, K. J. H., Sylwester, J., & Sylwester, B. 2013, *ApJ*, **768**, 135
 Karmakar, S. 2024, *AAS Meeting Abstracts*, 243, 447.06
 Karmakar, S., Naik, S., Pandey, J. C., & Savanov, I. S. 2022, *MNRAS*, **509**, 3247
 Kawai, H., Takao, Y., Tsuboi, Y., et al. 2017, *ATel*, 10753, 1
 Laming, J. M. 2015, *LRSP*, **12**, 2
 Laming, J. M. 2021, *ApJ*, **909**, 17
 Laming, J. M., Drake, J. J., & Widing, K. G. 1995, *ApJ*, **443**, 416
 Laming, J. M., Vourlidis, A., Korendyke, C., et al. 2019, *ApJ*, **879**, 124
 Lanza, A. F., Piluso, N., Rodonò, M., Messina, S., & Cutispoto, G. 2006, *A&A*, **455**, 595
 Linsky, J. L., Neff, J. E., Brown, A., et al. 1989, *A&A*, **211**, 173
 Maehara, H., Shibayama, T., Notsu, S., et al. 2012, *Natur*, **485**, 478
 Maehara, H., Shibayama, T., Notsu, Y., et al. 2015, *EP&S*, **67**, 59
 Mullan, D. J., Mathioudakis, M., Bloomfield, D. S., & Christian, D. J. 2006, *ApJS*, **164**, 173
 Muneer, S., Jayakumar, K., Rosario, M. J., Raveendran, A. V., & Mekkaden, M. V. 2010, *A&A*, **521**, A36
 Namekata, K., Maehara, H., Honda, S., et al. 2021, *NatAs*, **6**, 241
 Nordon, R., & Behar, E. 2007, *A&A*, **464**, 309
 Nordon, R., & Behar, E. 2008, *A&A*, **482**, 639
 Osten, R. A., Brown, A., Ayres, T. R., et al. 2004, *ApJS*, **153**, 317
 Pandey, J. C., & Singh, K. P. 2008, *MNRAS*, **387**, 1627
 Pandey, J. C., & Singh, K. P. 2012, *MNRAS*, **419**, 1219
 Perdelwitz, V., Navarrete, F. H., Zamponi, J., et al. 2018, *A&A*, **616**, A161
 Reale, F. 2007, *A&A*, **471**, 271
 Reale, F. 2014, *LRSP*, **11**, 4
 Reale, F., Betta, R., Peres, G., Serio, S., & McTiernan, J. 1997, *A&A*, **325**, 782
 Seli, B., Oláh, K., Kriskovics, L., et al. 2022, *A&A*, **659**, A3
 Serio, S., Reale, F., Jakimiec, J., Sylwester, B., & Sylwester, J. 1991, *A&A*, **241**, 197
 Singh, G., & Pandey, J. C. 2024, *ApJ*, **966**, 86
 Smith, R. K., Brickhouse, N. S., Liedahl, D. A., & Raymond, J. C. 2001, *ApJL*, **556**, L91
 Strassmeier, K. G., & Bartus, J. 2000, *A&A*, **354**, 537
 Strüder, L., Briel, U., Dennerl, K., et al. 2001, *A&A*, **365**, L18
 To, A. S. H., Long, D. M., Baker, D., et al. 2021, *ApJ*, **911**, 86
 Tsuboi, Y., Yamazaki, K., Sugawara, Y., et al. 2016, *PASJ*, **68**, 90
 Turner, M. J. L., Abbey, A., Arnaud, M., et al. 2001, *A&A*, **365**, L27
 Veronig, A., Temmer, M., Hanslmeier, A., Otruba, W., & Messerotti, M. 2002, *A&A*, **382**, 1070
 Wilms, J., Allen, A., & McCray, R. 2000, *ApJ*, **542**, 914
 Wood, B. E., Laming, J. M., & Karovska, M. 2012, *ApJ*, **753**, 76
 Wood, B. E., & Linsky, J. L. 2010, *ApJ*, **717**, 1279
 Yan, Y., He, H., Li, C., et al. 2021, *MNRAS*, **505**, L79
 Yashiro, S., & Gopalswamy, N. 2009, in *IAU Symp. 257, Universal Heliophysical Processes*, ed. N. Gopalswamy & D. F. Webb (Cambridge: Cambridge Univ. Press), 233
 Zimovets, I. V., Sharykin, I. N., & Gan, W. Q. 2020, *ApJ*, **891**, 138